ACS SENSORS

pubs.acs.org/acssensors

Article

Insights into the Formation of DNA–Magnetic Nanoparticle Hybrid Structures: Correlations between Morphological Characterization and Output from Magnetic Biosensor Measurements

Reinier Oropesa-Nuñez,* Teresa Zardán Gómez de la Torre, Henry Stopfel, Peter Svedlindh, Mattias Strömberg, and Klas Gunnarsson*

Cite This: *ACS Sens.* 2020, 5, 3510–3519

Read Online

ACCESS | Metrics & More | Article Recommendations | Supporting Information

ABSTRACT: Understanding the binding mechanism between probe-functionalized magnetic nanoparticles (MNPs) and DNA targets or amplification products thereof is essential in the optimization of magnetic biosensors for the detection of DNA. Herein, the molecular interaction forming hybrid structures upon hybridization between DNA-functionalized magnetic nanoparticles, exhibiting Brownian relaxation, and rolling circle amplification products (DNA-coils) is investigated by the use of atomic force microscopy in a liquid environment and magnetic biosensors measuring the frequency-dependent magnetic response and the frequency-dependent modulation of light transmission. This approach reveals the qualitative and quantitative correlations between the morphological features of the hybrid structures with their magnetic response. The suppression of the high-frequency peak in the magnetic response and the appearance of a new peak at lower frequencies match the formation of larger sized assemblies upon increasing the concentration of DNA-coils. Furthermore, an increase of the DNA-coil concentration induces an increase in the number of MNPs per hybrid structure. This study provides new insights into the DNA–MNP binding mechanism, and its versatility is of considerable importance for the mechanistic characterization of other DNA-nanoparticle biosensor systems.

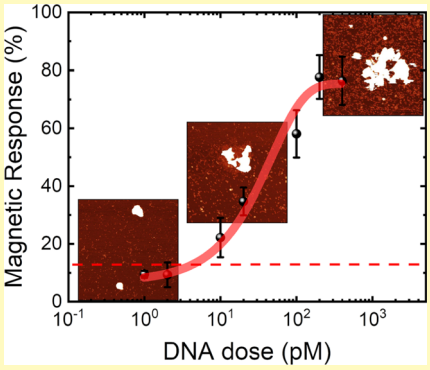

KEYWORDS: *DNA–magnetic nanoparticle hybrid structures, atomic force microscopy, magnetic biosensing, rolling circle amplification products, volume-amplified magnetic nanobead detection assay*

Early diagnosis and efficient monitoring of pathogen spread are important features during the outbreaks of emerging infectious diseases.[1,2] Hence, there is an increasing demand for the development of highly specific, fast, and cost-efficient biosensor technologies to meet present and future needs in different fields, including medicine,[3−7] food safety applications,[8−10] and environmental monitoring.[11,12] The detection of different pathogens and biomarkers at the point-of-care (POC) benefits from the rapid detection of specific biomolecules like DNA sequences and proteins.

Approaches based on acoustic,[13−15] electrochemical,[11,16,17] optical,[18−20] and magnetic[21−27] readout strategies have been used for the development of new POC and out-of-lab biosensor technologies. In particular, analytical techniques based on magnetic nanoparticles (MNPs) as readout labels have attracted considerable attention in the past two decades because of the improvements in the synthesis and functionalization of MNPs.[28−30] MNPs offer unique advantages for biosensing. First, MNPs provide a sensing platform with a low background signal, that is, a high signal-to-noise ratio because most biological samples do not contribute with any detectable magnetic background.[31] Second, MNPs exhibit highly stable physical properties that can be detected using low-cost instrumentation.[32,33] Third, MNPs are relatively inexpensive to produce. Fourth, MNPs can be manipulated by external magnetic fields providing the possibility to perform target enrichment before quantification, thereby increasing the sensitivity of the biosensor.[34] Finally, MNPs typically consist of a core made of a magnetic material and a non-magnetic biopolymer casing which provides colloidal stability and enables surface functionalization with different biomolecular probes, thereby allowing for their integration in sensing devices to detect a wide range of biomarkers.[35−37]

Two categories have been established to classify magnetic biosensors measuring the magnetic signal from MNPs.[38] The first category, the substrate-based technology, measures the signal change induced by the binding of the biofunctionalized MNPs to a sensor surface when the target molecule is

Received: August 5, 2020
Accepted: October 20, 2020
Published: November 3, 2020

https://dx.doi.org/10.1021/acssensors.0c01623
ACS Sens. 2020, 5, 3510–3519

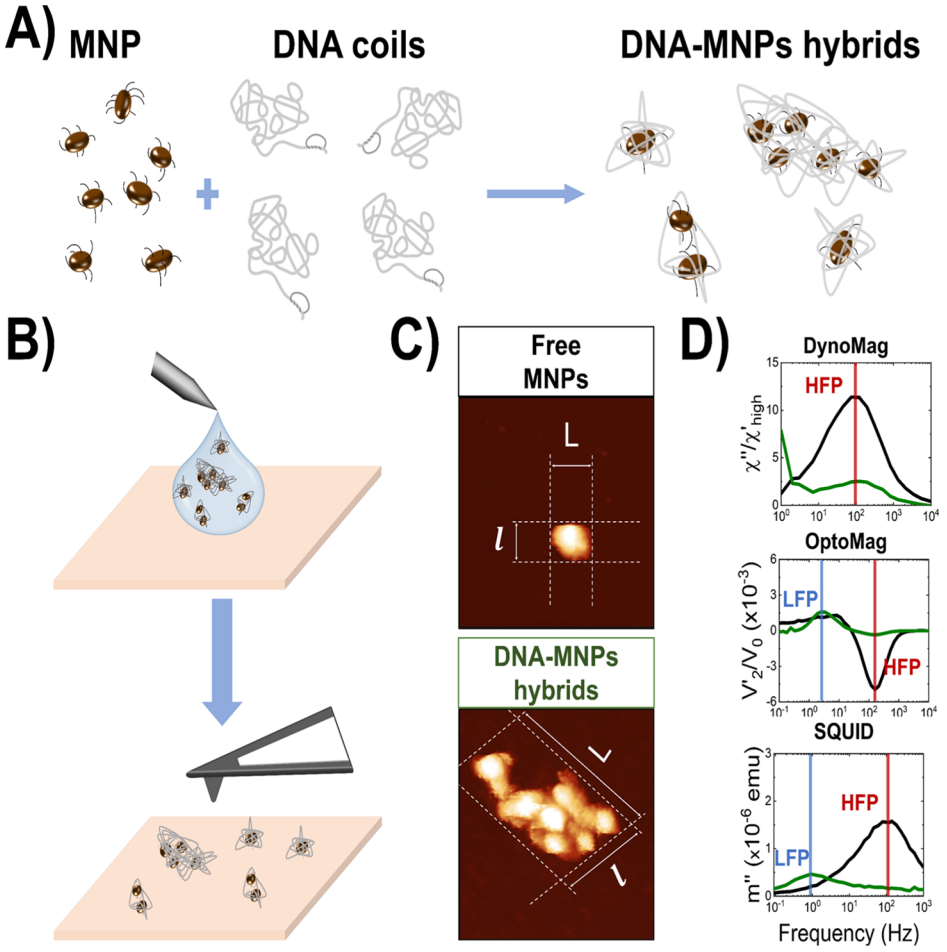

Figure 1. Schematic description of the methodology followed in the present study. Functionalized-MNPs are incubated with DNA-coils to form hybrid structures (A). DNA−MNP assemblies are then deposited onto mica substrates and characterized by AFM in liquid (B). In (C), the approach to determine the hybrid sizes from the AFM imaging is presented using two representative examples of the structures formed for 0 pM (free MNPs) and 200 pM of DNA-coils (DNA−MNP hybrids). The average value between the long (L) and short (l) axis is used to estimate the hybrid size from AFM measurements. The results are compared with the magnetic response of the DNA−MNP assemblies (D), where the high-frequency and low-frequency peaks (HFP and LFP, respectively) are used to calculate the hydrodynamic diameter (D_h) of the hybrids.

present.[39−41] In contrast, the substrate-free (lab-on-a-bead) technology recognizes the change of the dynamic (frequency-dependent) magnetic response of the MNPs as they bind to the target or amplification products thereof.[42−44] Within this category, the volume-amplified magnetic nanobead detection assay (VAM-NDA) is a promising MNP-based bioassay for low-cost and easy-to-use diagnostic devices.[24,38,45−48] It measures the highly specific interaction between rolling circle amplification products (DNA-coils) and the complementary sequences of the oligonucleotide-functionalized MNPs once the sample is placed in an oscillating magnetic field.[49] As a result of such an interaction, DNA−MNP hybrid structures are formed where each oligonucleotide-functionalized MNP binds specifically the DNA-coils. Because of the increased size of DNA−MNP hybrid structures in comparison to free MNPs, the frequency-dependent magnetic response of the former will be shifted to lower frequency.

The unique features of atomic force microscopy (AFM) have been exploited in the last decades for morphological investigations of the nanostructured materials at a sub-nanometer resolution.[50,51] AFM is one of the several microscopy techniques that have been employed to study the interaction between DNA and MNPs.[52−57] AFM provides three-dimensional images with a high spatial resolution, comparable with that obtained by transmission electron microscopy (TEM) but without damaging soft samples (i.e., DNA-coils). Besides, unlike other well-established tools, for example, scanning electron microscopy (SEM), TEM, and conventional optical microscopy, AFM does not require coating or labeling of the sample, which is an advantage for understanding the underlying binding mechanisms for the formation of DNA−MNP hybrid structures. In particular, AFM has been used to characterize the morphology of *Escherichia coli* DNA-coils formed by rolling circle amplification[58] and also to investigate the effect of an inert electrolyte in the interaction between calf thymus double-stranded DNA (dsDNA) and nonfunctionalized gold nanoparticles.[55] Additionally, this technique was used to demonstrate that the decrease in the spin−spin relaxation time of water protons observed in NMR measurements can be ascribed to the oligomerization of iron oxide nanoparticles upon hybridization with the target DNA sequence.[56] However, most of these studies, similar to those employing TEM, were performed by drying the samples before the measurements, thus hindering detailed structural information that can be obtained without the drying process. In this context, the proven versatility of

https://dx.doi.org/10.1021/acssensors.0c01623
ACS Sens. 2020, 5, 3510−3519

AFM of being capable to work under different environmental conditions offers a unique opportunity to overcome this drawback. In particular, by performing the AFM in a liquid environment, one avoids the capillary forces that originate from the humid coverage of both the sample and tip when performing the measurement in air. Liquid AFM is therefore capable of producing high-quality AFM images which may contribute to a better understanding of DNA−MNP hybrid formation under conditions in which the VAM-NDA assay is performed.

Understanding the interaction between the functionalized nanoparticles and target biomolecules is crucial for further improving the sensitivity of magnetic biosensors; the present study aims to provide further knowledge in this research field. For this purpose, we perform morphological characterization of DNA−MNP hybrid structures at different DNA-coil concentrations using AFM in liquid environments and correlate, qualitatively and quantitatively, these results with the results obtained from magnetic measurements in three different experimental setups. Our approach provides imaging of DNA−MNP hybrid structures in liquid environments with a high and unprecedented resolution. These findings increase the understanding of the underlying physicochemical mechanisms of magnetic biosensing in the VAM-NDA.

RESULTS AND DISCUSSION

Figure 1 shows a schematic representation of the approach used in this study. DNA−MNPs hybrid structures (Figure 1A) were deposited on mica substrates treated with the $NiCl_2$ solution, and their morphological features were characterized by AFM (Figure 1B). As expected from the fact that the MNPs are of a multicore type, they exhibit irregular shapes.[38] The size of a DNA−MNP hybrid structure observed by AFM was defined as

$$D_{AFM} = \frac{(L + l)}{2} \quad (1)$$

where L and l are the long axis and short axis lengths, respectively (Figure 1C). The AFM data were compared with results from frequency-dependent magnetic measurements of samples containing hybrid structures (Figure 1D).

The morphological characterization of DNA−MNP hybrid structures, prepared from four different DNA-coil concentrations (0, 2, 20, and 200 pM) and a constant MNP concentration (100 μg/mL), shows a trend for hybrid structures to cluster with increasing DNA-coil concentration (Figure 2). In particular, the formation of larger assemblies was observed for DNA-coil concentrations of 20 and 200 pM. In contrast, the hybrids formed in the case of 2 pM DNA concentration resembled the structures found in the negative control sample (NC, 0 pM). The AFM micrographs also show the progressive accumulation of DNA-coils onto the mica substrate with increasing DNA-coil concentration. A clean background was observed in the absence of DNA-coils. Noteworthy, the highly specific and strong (base-paired) interactions between the DNA-coils and the oligonucleotide-functionalized MNPs results in DNA−MNP hybrid structures that can withstand several hours of AFM measurements without damage to their morphologies. Additional AFM images of the hybrid structures are shown in Figure S1 and S2.

Detailed information on the mechanism of interaction between MNPs and DNA-coils was deduced from micrographs acquired at higher lateral resolution. At low DNA-coil concentration (2 pM), only a few DNA-coils interacting with MNPs can be observed, binding externally to or coiling around MNPs (Figure 3A). As expected, an increasing number of DNA-coils binds to each MNP with increasing DNA-coil concentration. Also, assemblies where one MNP is bound to several DNA-coils were detected (Figure 3B,C). The DNA-coils with bound MNPs were observed as coiled molecules as

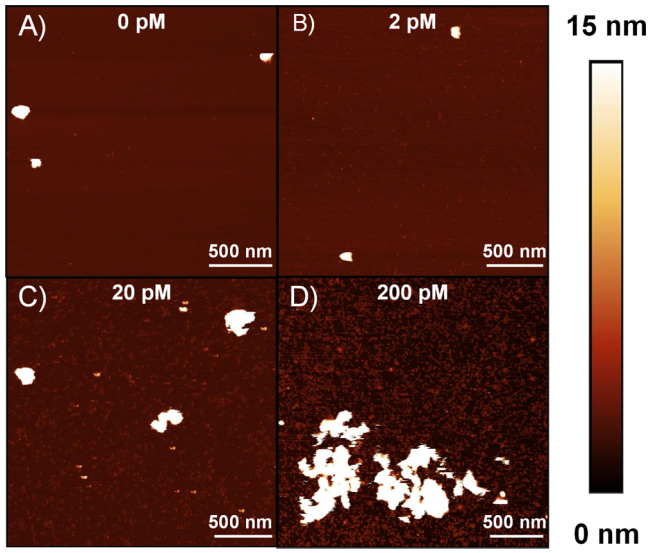

Figure 2. AFM images of DNA−MNP hybrid structures formed in the absence (A) and the presence of randomly coiled DNA (B−D). The hybrid size increases with the increase of DNA-coil concentration showing cluster formation for the 20 pM (C) and 200 pM (D) samples. This effect is not observed for the 2 pM (B) samples where the hybrid structures, albeit showing a slight increase in the D_{AFM} values, resemble the unbound MNPs in the absence of DNA-coils (A).

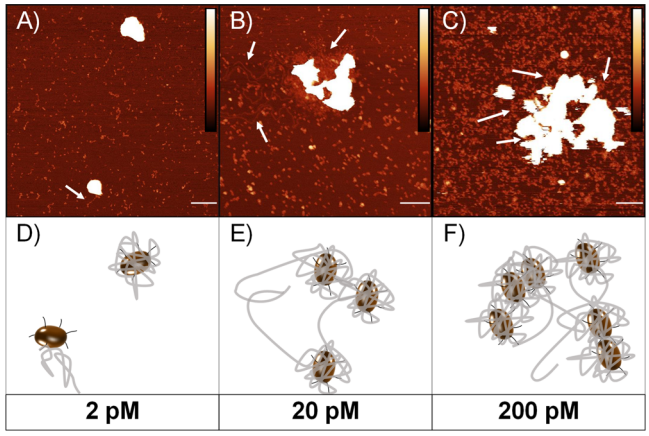

Figure 3. AFM micrographs at higher magnifications of the DNA−MNPs hybrid structures formed in the presence of randomly coiled DNA (A−C). MNPs scarcely interact with DNA-coils at 2 pM (A). This interaction is favored by increasing the DNA-coil concentration to 20 pM (B) and 200 pM (C) where more DNA-coils per MNPs are observed. The AFM images confirm the cluster formation at higher DNA concentrations showing hybrid structures containing a larger number of DNA-coils, which in some cases act as "bridges" between assemblies. Some DNA-coils are highlighted with white arrows. The color bars correspond to a Z range of 10.0 nm. Scale bars: 200 nm. Schematic representations of typical arrangements of hybrid structures as observed by the AFM images are also presented (D−F).

https://dx.doi.org/10.1021/acssensors.0c01623
ACS Sens. 2020, 5, 3510−3519

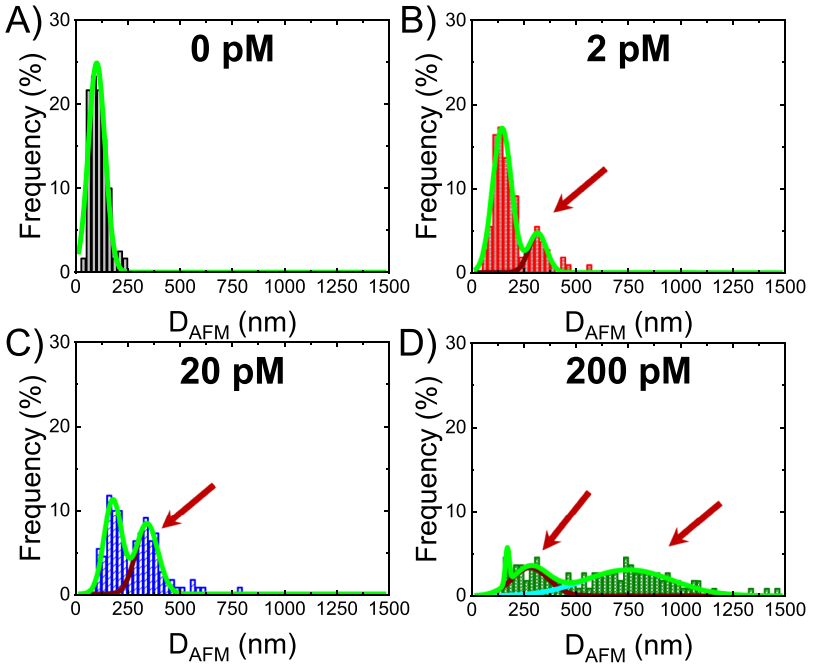

Figure 4. D_{AFM} distributions, fitted with Gaussian functions, of the different hybrid structures. In the absence of DNA-coils (A) only one size distribution, attributed to free (unbound) MNPs, is observed, while a second size population around 300 nm (red arrows) emerges from the 2 pM sample (B). This finding is also perceived for the 20 pM sample (C) where both size populations display similar probabilities. The D_{AFM} distribution is broader in the case of the 200 pM sample (D).

Table 1. Comparison between the Gaussian-Fitted D_{AFM} Values and the Calculated Hydrodynamic Diameter D_h derived from the AC Susceptometry Outputs

	D_{AFM}[a] (nm)			DynoMag D_h (nm)		Optomagnetic D_h (nm)		SQUID D_h (nm)	
[DNA] (pM)	peak 1	peak 2	peak 3	HFP	LFP	HFP	LFP	HFP	LFP
0	101 ± 80			171 ± 13		112 ± 16		163 ± 16	
2	145 ± 91	315 ± 84		171 ± 13		112 ± 16		163 ± 16	
20	180 ± 84	343 ± 106		171 ± 13		112 ± 16	331 ± 48	163 ± 16	
200	170 ± 18	280 ± 173	749 ± 415	171 ± 13		112 ± 16	444 ± 63	163 ± 16	792 ± 82

[a](Peak mean value ± FWHM).

well as thread-like objects (Figure 3B). In the case of 200 pM DNA-coil concentration, the DNA-coils even acted as "bridges" between the different assemblies (Figure 3C). Figure 3D–F provides a schematic illustration of the MNP-DNA-coil interaction for different DNA-coil concentrations based on the obtained AFM results.

The DNA–MNP hybrid size distribution was obtained by analyzing a large number of hybrid structures ($N \geq 110$) and by acquiring more than 10 AFM images for each DNA–MNP hybrid structure. The average size D_{AFM} of the structures increased from 108 ± 41 nm in the absence of DNA-coils to 191 ± 95 nm for the 2 pM sample. In the case of hybrids prepared from DNA-coil concentrations of 20 and 200 pM, the D_{AFM} values were 280 ± 125 and 607 ± 307 nm, respectively. This result was expected considering that the number of DNA-coils bound to MNPs should increase with increasing DNA-coil concentration, consequently increasing the size of the hybrid structures.

An important insight into the binding mechanism of DNA-coils with MNPs was deduced from the fitting of the D_{AFM} histograms with Gaussian functions (Figure 4). In the absence of DNA-coils, the MNPs show a D_{AFM} distribution centered around 100 nm (Figure 4A). The intensity of this peak decreases with increasing DNA-coil concentration (Figure 4B–D), showing a remarkable difference between 0 and 200 pM DNA-coil concentrations. The peak located at ∼100 nm for the latter was drastically diminished (Figure 4D). Interestingly, a second peak in the size distribution, peaking at around 300 nm, emerged for the 2 pM sample (highlighted by a red arrow in Figure 4B). The same behavior was observed for the assemblies prepared from the 20 pM DNA-coil concentration sample (Figure 4C). In this case, the peak amplitude for hybrid structures having sizes around 300 nm was higher indicating a higher probability of finding such sizes for this sample. Furthermore, for the 20 pM sample, the number of hybrid structures having a size of 100 nm or 300 nm, showed similar values in terms of frequency. A more complex scenario was observed in the case of the 200 pM sample. Figure 4D shows a wide D_{AFM} distribution, exhibiting peaks around 170, 300, and 750 nm. The number of DNA–MNP hybrid structures of the population centered at 750 nm represents 72% (because it is a broad peak ranging from 350 to 1500 nm) of the total size distribution; however, the peak amplitude is not predominant over the other peaks. The output from fitting Gaussian functions to the D_{AFM} distributions are summarized in Table 1.

To assess whether our findings could be potentially applied for optimizing the performance of MNP-based biosensors, we

https://dx.doi.org/10.1021/acssensors.0c01623
ACS Sens. 2020, 5, 3510–3519

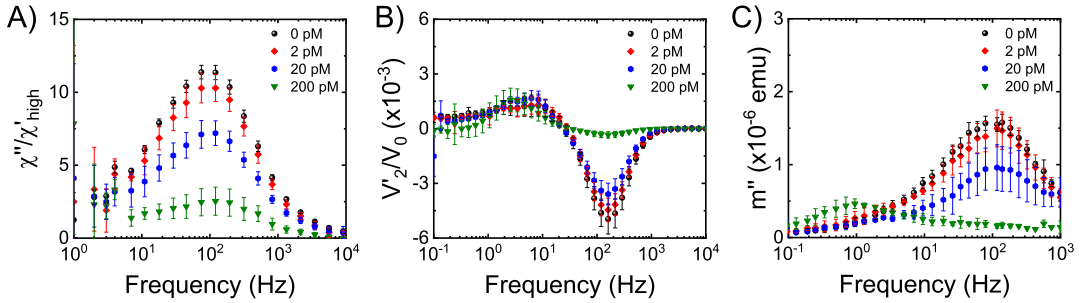

Figure 5. Frequency-dependent magnetic response for the different hybrid structures (A–C). Out-of-phase component (imaginary part) of the AC susceptibility versus frequency measured using a DynoMag susceptometer (A) and SQUID magnetometer (C), as well as the frequency-dependent in-phase component of the complex second harmonic of the transmitted light measured with the optomagnetic readout (B). A drop in the signal because of a decreasing concentration of free MNPs with the increase of DNA-coil concentration is confirmed at higher relaxation frequencies for all the readouts. A new peak at lower relaxation frequencies is resolved for 20 and 200 pM samples in an optomagnetic sensor (B), while this peak is only observed for the 200 pM sample in the SQUID measurements (C).

recorded the frequency-dependent complex magnetization for the same four DNA-coil concentrations used in the AFM study (0, 2, 20 and 200 pM). Three different experimental platforms exploiting volumetric sensing were used. Since the MNPs used in our study exhibit blocked magnetic moments, the physical rotation of the particle (Brownian relaxation) is the dominating relaxation mechanism. The characteristic frequency for Brownian relaxation dynamics, for MNPs having a mean hydrodynamic diameter (D_h), is expressed as

$$f_B = \frac{k_B T}{\pi^2 \eta {D_h}^3} \tag{2}$$

where η is the dynamic viscosity of the carrier liquid and $k_B T$ is the thermal energy.[24,26,27,59]

The frequency-dependent imaginary part of the complex magnetic susceptibility (χ'') exhibits a peak in the frequency range between 75 and 121 Hz (Figure 5A). As expected, the peak amplitude diminishes with increasing DNA-coil concentration because of that the number of immobilized MNPs becomes higher. A similar DNA-coil concentration dependence was observed when the real part (V_2') of the complex second harmonic signal of the transmitted light intensity was measured. The immobilization of MNPs to the DNA coils affected the amplitude of the peak found at ∼160 Hz, significantly decreasing the V_2'/V_0 values (Figure 5B). Cluster formation was detected for the 20 pM sample from the appearance of a new peak between 4 and 8 Hz. This peak was also observed for the 200 pM sample and shifted toward lower frequency values (1.5–3.5 Hz).

To evaluate if the low-frequency peak in the optomagnetic spectra can be detected as a corresponding relaxation peak in the complex AC susceptibility spectrum, the imaginary part of the complex magnetization (m'') was acquired using a superconducting quantum interference device (SQUID) magnetometer (Figure 5C) because the frequency range of the AC susceptometer is limited to 1 Hz with considerable influence of measurement noise between 1 and 5 Hz. A frequency range between 0.1 and 1 kHz was used in order to measure the low-frequency peak. Figure 4C shows the decrease in the amplitude of the peak found at high frequencies (120–180 Hz) by increasing the DNA-coil concentration. The low-frequency peak located at 1 Hz was detected in the 200 pM sample. However, no peak at lower frequencies was resolved for the 20 pM sample.

Considering the presence of peaks at high and low frequencies (denoted HFP and LFP, respectively), the D_h of the different hybrid structures was calculated using eq 2. Here, it was assumed that the DNA–MNP assemblies have spherical shapes. Noteworthy, in the case of the optomagnetic measurements, the Brownian relaxation frequency at low magnetic fields in the linear response regime is related to the peak frequency as[59]

$$f_{peak} \approx \frac{1.21}{\sqrt{3}} f_B \tag{3}$$

Table 1 summarizes the corresponding D_h values. The difference in the DynoMag and SQUID values for D_h is within the limits of experimental error, while the optomagnetic values are considerably smaller corresponding to a larger than expected value for the extracted Brownian relaxation frequency. The explanation for this difference can be found in the magnetic field amplitudes used in the different measurements. While the DynoMag and SQUID measurements use a magnetic field amplitude of 0.5 and 0.4 mT, respectively, the optomagnetic measurement uses a considerably larger value for the magnetic field amplitude (2.6 mT) to increase the signal-to-noise ratio. The used field amplitude is outside the linear response regime for the measurement, resulting in V_2'/V_0 versus frequency curves shifted toward a higher frequency.[60,61] The optomagnetic measurement thus overestimates the Brownian relaxation frequency (underestimates the value for D_h).

The analytical performance of AC susceptometry methods depends on the magnetic readout sensitivity and the interplay between MNPs and the target molecules. Optimal magnetic biosensors should have a short total assay time, a low contamination risk, and the potential for automation as crucial properties for *in situ* decentralized diagnostics.[62,63] Furthermore, the detection of low concentrations of MNPs is essential to improve the sensitivity of the bioassay.[64] Experimental evidence indicates that the interaction between MNPs and DNA coils has a primary role in optimizing DNA-based magnetic biosensors because its comprehension is required for the proper understanding of the underlying detection mechanism.[23,24,38]

The first important finding of the present study is that an increased DNA-coil concentration induces an increase of the arithmetic D_{AFM} values. The D_{AFM} values obtained for the different DNA-coil concentrations followed the ranking

https://dx.doi.org/10.1021/acssensors.0c01623
ACS Sens. 2020, 5, 3510–3519

D_{AFM}(0 pM) < D_{AFM}(2 pM) < D_{AFM}(20 pM) < D_{AFM}(200 pM), which is in good correlation with the decrease of the HFP amplitude with increasing DNA-coil concentration and with the trend observed in the dynamic light scattering (DLS) measurements (Figure S3). Moreover, the cluster formation, mainly observed for the samples with DNA-coil concentrations of 20 and 200 pM (Figures 2C,D, and S1), is in good agreement with the large decrease of the HFP amplitudes recorded in the different magnetic readout methods (Figure 5). The formation of such large assemblies was also detected as the appearance of an LFP located at frequencies below 10 Hz for both the 20 and 200 pM samples (Figure 5B,C). The latter was also observed in the DLS measurements with the appearance of a peak at larger hydrodynamic diameters (Figure S3). The formation of such assemblies was not observed in the case of the 2 pM sample, neither in the AFM or the magnetic measurements, resembling more the results found in the NC sample. All these observations lead us to conclude that there exists a strong correlation between (i) the DNA-coil concentration, (ii) the average size of the hybrid structures determined by AFM, and (iii) the amplitude of the HFP commonly associated with the free (unbound) MNPs. It must be considered that the length and conformation of the DNA targets may play a role in the morphology of DNA−MNP hybrids. However, no significant differences were observed in the AC susceptometry results nor in the DNA−MNP hybrid morphology when the 200 pM samples were investigated using three different DNA-coil lengths (Figure S4). The latter confirms previous observations where long amplification time was not required to detect low concentrations of target DNA.

Another interesting observation is the agreement between the Gaussian-fitted D_{AFM} distributions and the calculated D_h values derived from the different magnetic measurements (Table 1). This result can be ascribed to the approach employed in this study. First, the selection of the ScanAsyst mode to perform AFM imaging in liquid provides high-quality images avoiding imaging artifacts. Second, the treatment of the mica substrate with Ni^{2+} cations implies weak electrostatic attachment of the DNA coils and DNA−MNP hybrid structures to the surface, which favors AFM imaging of the assemblies under conditions similar to those of magnetic biosensor measurements. Finally, the deposition protocol that was performed without drying the samples and carried out during the first 2 h after hybridization, thereby avoiding the sedimentation of large aggregates observed by naked eye 3 h after hybridization in samples with higher DNA-coil concentration. To the best of our knowledge, this is the first time that such an agreement between Gaussian-fitted D_{AFM} distributions and the D_h values is reported, clearly indicating that our approach can be established as a methodology to study the interaction between DNA coils and functionalized MNPs in volumetric sensors.

An important outcome arising from our study is that an increase in DNA-coil concentration produces an increase in the number of MNPs per hybrid structure. Because the MNP concentration was kept constant for all four samples, an increase in DNA-coil concentration implies an increase in the number of DNA-coils available for each MNP. The latter is confirmed by the excess of DNA coils found in the background of the AFM micrographs (Figures 2, 3, and S1), and it is in agreement with previous findings.[24,38] From our AFM results, hybrid structures where one DNA coil binds to one MNP were found for the 2 pM sample (Figures 2B, 3A). A clear increase in the number of DNA coils per MNP was observed for the 20 and 200 pM samples as well as cluster formation by hybrid intergrowth in the latter (Figures 2, 3, and S1). Moreover, dividing the D_{AFM} values of the different hybrid structures by the D_{AFM} value of the free MNPs (0 pM sample), we obtain 1.7, 2.6, and 5.6 for the 2, 20, and 200 pM samples, respectively. The latter can be considered as an indication of the number of MNPs per hybrid structure, implying the presence of 1−2 MNPs per hybrid structure in the case of the 2 pM sample. This number increased to 2−3 and 5−6 MNPs in the cases of the 20 and 200 pM samples, respectively. Our results are in good agreement with previous findings, where it was demonstrated by transmission electron microscopy that each hybrid structure contained two MNPs.[38]

To explain all these findings, we considered two different scenarios. The first assumes the DNA coils bound to one MNP as the cause of the increase of D_{AFM} for hybrid structures, and consequently, the decrease of the HFP amplitude, upon increasing the DNA-coil concentration. This hypothesis has long been recognized by the scientific community.[24,38,52] However, it does not explain the morphologies of the hybrid structures found in samples with higher DNA-coil concentrations. In the second scenario, it is conjectured that an increase in DNA-coil concentration during the hybridization promotes the binding between MNPs and DNA-coils already bound to other MNPs. The latter is supported by the DNA "bridges" linking smaller assemblies observed for the 200 pM samples (Figures 2D, 3C). According to our AFM results, such DNA "bridges" may be formed as follows. At a low concentration (2 pM), DNA-coils are either wrapped around MNPs (cf. Figure 3D upper right) or bound to MNPs without saturation of all binding sites (cf. Figure 3D lower left). The former may explain the slight increase of the D_{AFM} values corresponding to peak 1 (cf. Table 1 and Figure 4). Increasing the number of DNA coils (20 pM) will result in an increasing number of DNA coils bound to each MNP. Furthermore, the coupling between free MNPs and DNA coils already bound to another MNP (cf. Figure 3E) is also favored. This explains the formation of small DNA−MNP hybrid structures containing two or more MNPs, which is consistent with the appearance of peak 2 (cf. Figure 4 and Table1). Noteworthy, the formation of such assemblies is not excluded for the 2 pM samples. However, because the DNA-coil concentration is lower, the probability of finding such structures is lower compared to the 20 pM samples. At higher DNA-coil concentrations (200 pM), large hybrid structures tend to form by the aggregation of smaller DNA−MNP hybrids (cf. Figure 3F). DNA coils act as "bridges" between different DNA−MNP hybrids. In one case, the hybrids are connected via free DNA coils that bind to MNPs which are embedded in different DNA−MNP hybrids (hybrid bound to free DNA bound to hybrid). In another case, the aggregation results from the binding between a DNA coil already coupled to a DNA−MNP hybrid and a MNP with the available binding sites present in another hybrid (hybrid bound to hybrid). Considering all the above, we conclude that a combination of both scenarios provides a better comprehension of the binding mechanisms between MNPs and DNA coils, where the diffusion of DNA coils and MNPs seems to play a key role.

CONCLUSIONS

In this work, we applied AFM in liquid environments to characterize, with unprecedented resolution, the morphological

https://dx.doi.org/10.1021/acssensors.0c01623
ACS Sens. 2020, 5, 3510−3519

features of hybrid structures formed by the interaction between MNPs and four different DNA-coil concentrations. We showed that higher DNA-coil concentrations induce cluster formation, which is related to the decrease of the magnetic response at frequencies corresponding to the Brownian relaxation frequency of free MNPs. By correlating the results derived from the AFM analysis with the outputs from the three different magnetic readout systems, we have provided a better understanding of the binding characteristics between MNPs and DNA coils in the VAM-NDA. Because of the versatility of the tools employed in our approach, it may be extended to other applications where the interaction mechanism between nanoparticles and target molecules or amplification products thereof must be addressed. Furthermore, we also provide our interpretation of the binding mechanisms occurring between MNPs and DNA coils indicating that the diffusion of DNA coils and MNPs should be considered for future optimizations of the VAM-NDA.

EXPERIMENTAL SECTION

Materials. Adenosine triphosphate (ATP), bovine serum albumin (BSA), deoxynucleoside triphosphate (dNTP), T4 ligase, Φ29 DNA polymerase, and reaction buffer for Φ29 DNA polymerase were purchased from Thermo Scientific (Vilnius, Lithuania). *Vibrio cholerae* oligonucleotide sequences were acquired from Biomers GmbH (Ulm, Germany). All used oligonucleotide sequences are presented in Table S1. Streptavidin functionalized 100 nm Bionized NanoFerrite (BNF)-starch particles (cluster-type, product code 10-19-102) were purchased from Micromod Partikeltechnologie GmbH (Rostock, Germany). Phosphate-buffered saline (PBS, ultrapure grade) was purchased from AMRESCO (Solon, USA). Nickel chloride ($NiCl_2$), sodium chloride (NaCl), ethylenediaminetetraacetic acid (EDTA), ultrapure 1 M Tris−HCl (pH 8.0) buffer, Tween 20, and HEPES were purchased from Sigma-Aldrich.

Preparation of DNA-Coils. The target recognition, ligation, and RCA were performed according to previously detailed protocols.[24,46] Details are given in Supporting Information. A stock solution of RCA products (4 nM, considering the initial concentration of the padlock probes) was stored at 4 °C for use.

Conjugation of Magnetic Nanoparticles with Detection Probes. A stock solution of MNPs (10 mg/mL, 3.2 g/ccm, 6×10^{12} beads/mL) conjugated with a 60-fold oligonucleotide excess was produced following a protocol described elsewhere.[24] Briefly, 40 μL of streptavidin-modified BNF-starch particles were washed twice in a washing buffer (10 mM Tris−HCl (pH 8.0), 5 mM EDTA, 0.1% (v/v) Tween 20, and 0.1 M NaCl) using a magnetic separation stand. Noteworthy, the MNPs consist of a 75−80% (w/w) cluster-type core of magnetite and a cross-linked shell of hydroxyl starch possessing a magnetization of 49 Am^2/kg iron (H = 80 kA/m) and a saturation magnetization higher than 76 Am^2/kg iron (H > 800 kA/m). The MNPs have a biotin binding capacity of >300 pmol/mg iron), and the particles were conjugated by adding 2.49 μL of a 10 μM biotinylated oligonucleotide probe (Table S1) solution followed by 15 min of incubation at room temperature. Finally, the MNP suspension was washed twice with 1× PBS buffer and resuspended to a final concentration of 10 mg/mL in PBS. The MNP suspension was stored at 4 °C until use.

Preparation of DNA−MNP Hybrid Structures. For the detection of *V. cholerae* DNA coils, 20 μL of oligonucleotide tagged MNPs (1 mg/mL) were gently mixed with 20 μL of DNA-coil solution (0, 20, 200, and 2000 pM, defined by the initial concentration of the padlock probes) in an Eppendorf tube. The mixture was incubated for 20 min at 55 °C in a heating block and, finally, diluted with 160 μL of PBS to a final volume of 200 μL. Noteworthy, the DNA concentrations were chosen based on the dose−response curves obtained from the magnetic outputs (see Figure S5). For instance, the 2 pM sample was picked to represent samples below the linear region of the dose response curve; while the 20 and 200 pM samples were chosen to represent samples in the linear and saturation regions of the dose response curve, respectively. The 0 pM sample (absence of DNA) depicts the characteristics of free MNPs.

Deposition Protocol for Hybrid Structures. The negatively charged mica substrates (G250-1, Agar Scientific Ltd., Essex, U.K.) were Ni^{2+}-treated to immobilize the DNA−MNP hybrid structures. A 20 μL aliquot of a buffered 10 mM $NiCl_2$ solution was deposited for 1 min onto a freshly cleaved mica substrate fixed to a glass slide. The substrate was then thoroughly rinsed with pure water (MilliQ, Millipore) and promptly dried with filter paper. Subsequently, a 20 μL droplet containing the hybrid structures was incubated for 1 min. Afterward, the sample was gently rinsed with 1 mL of imaging buffer (2 mM $NiCl_2$, 20 mM HEPES, pH 7.4). Noteworthy, the hybrid structures were deposited during the first 2 h after hybridization on the same day of their preparation to avoid cluster sedimentation.

AFM Imaging. The size and morphology characterization of the hybrid structures was conducted using a Bruker Dimension Icon atomic force microscope (Bruker Dimension Icon, Billerica, MA, USA). ScanAsyst mode in a liquid environment was employed for the measurements. V-shaped SNL silicon nitride cantilevers (Bruker, Billerica, MA, USA), with a typical tip curvature radius of 2−12 nm, nominal spring constant of 0.24 N/m, and resonance frequency in air ranging from 40 to 75 kHz were used. Scan areas of 10 × 10 μm^2 (1024 points per line) and 2.5 × 2.5 μm^2 (2048 points per line) were analyzed. The AFM images were processed using Gwyddion 2.54 software. The AFM size of the hybrid structures D_{AFM} was determined by measuring the long axis and short axis lengths (see Figure 1) according to eq 1.

The statistical analysis was performed on more than 110 hybrid structures for each DNA-coil concentration. It must be noted that the AFM imaging of the hybrid structures was always performed within the same day of their preparation.

AC Susceptometry. Dynamic magnetic measurements of the hybrid structures were carried out at room temperature using three different readout systems. A DynoMag AC susceptometer (Acreo Swedish ICT, Sweden), an optomagnetic measurement setup (details are given in Supporting Information), and a Superconducting Quantum Interference Device (SQUID) magnetometer (QD MPMS XL, Quantum Design, USA) were used to evaluate the frequency-dependent magnetic response for the different hybrid structures. In the case of the DynoMag setup, the frequency-dependent magnetic susceptibility ($\chi = \chi' - i\chi''$) was measured by acquiring 25 logarithmically equidistant points within the frequency range of 1 Hz to 100 kHz using an AC induction amplitude of 0.5 mT. The frequency range in the case of the optomagnetic measurement setup was 0.1 Hz to 10 kHz, and the AC induction amplitude was set at 2.6 mT to acquire 40 data points in 900 s. In this case, the modulation of the transmitted light intensity versus frequency for the hybrid structures was measured as the in- and out-of-phase second harmonic components of the photodetector voltage signal by applying the AC magnetic field perpendicular to the laser beam. For the SQUID measurements, the frequency range was 0.1 Hz to 1 kHz and the AC induction amplitude was 0.4 mT. Thirty-two logarithmically equidistant points were acquired. Details of the working principles for each of the used magnetic sensors are found elsewhere.[21,23,46,48,49] Sample volumes of 200 μL, taken from each one of the different hybrid structure suspensions, were pipetted into a 1 mL shell vial (Cat. No 548-0042, VWR international, Germany) and into a disposable UV-transparent cuvette (REF 67.758.001, SARSTEDT, Nümbrecht, Germany) for the DynoMag and optomagnetic measurements, respectively. In the case of SQUID measurements, the sample volume was 25 μL pipetted into a Teflon capsule. A minimum of three independent samples per DNA-coil concentration were analyzed for each magnetic measurement.

https://dx.doi.org/10.1021/acssensors.0c01623
ACS Sens. 2020, 5, 3510−3519

■ ASSOCIATED CONTENT

Supporting Information

The Supporting Information is available free of charge at https://pubs.acs.org/doi/10.1021/acssensors.0c01623.

In- and out-of-phase magnetic response versus frequency for DynoMag and optomagnetic setups, dose−response curves, additional AFM micrographs of DNA−MNP hybrid structures, dynamic light scattering (DLS) results, RCA protocol, and oligonucleotide sequences (PDF)

■ AUTHOR INFORMATION

Corresponding Authors

Reinier Oropesa-Nuñez − *Department of Materials Science and Engineering, Uppsala University, SE-751 03 Uppsala, Sweden*; orcid.org/0000-0002-9551-6565; Email: reinier.oropesa@angstrom.uu.se

Klas Gunnarsson − *Department of Materials Science and Engineering, Uppsala University, SE-751 03 Uppsala, Sweden*; Email: klas.gunnarsson@angstrom.uu.se

Authors

Teresa Zardán Gómez de la Torre − *Department of Materials Science and Engineering, Uppsala University, SE-751 03 Uppsala, Sweden*

Henry Stopfel − *Department of Materials Science and Engineering, Uppsala University, SE-751 03 Uppsala, Sweden*

Peter Svedlindh − *Department of Materials Science and Engineering, Uppsala University, SE-751 03 Uppsala, Sweden*

Mattias Strömberg − *Department of Materials Science and Engineering, Uppsala University, SE-751 03 Uppsala, Sweden*; orcid.org/0000-0003-0648-3130

Complete contact information is available at: https://pubs.acs.org/10.1021/acssensors.0c01623

Author Contributions

R.O.-N. designed and performed the experiments, analyzed the data, and wrote the manuscript. T.Z.G.d.l.T. and H.S. helped in performing the experiments and wrote the manuscript. P.S. designed and supervised the study and wrote the manuscript. M.S. designed and supervised the study, analyzed the data, and wrote the manuscript. K.G. designed and supervised the study, analyzed the data, and wrote the manuscript.

Notes

The authors declare no competing financial interest.

■ ACKNOWLEDGMENTS

Olle Engkvist (project number 194−0644), FORMAS (project number 221-2014-574), the Swedish Foundation for Strategic Research (SSF project FLU-ID), and the Uppsala Antibiotic Center are gratefully acknowledged for financial support.

■ ABBREVIATIONS

AFM, atomic force microscopy; DNA, deoxyribonucleic acid; MNPs, magnetic nanoparticles; NC, negative control; POC, point-of-care; RCA, rolling circle amplification; SQUID, superconducting quantum interference device; TEM, transmission electron microscopy; VAM-NDA, volume-amplified magnetic nanobead detection assay

■ REFERENCES

(1) Ellwanger, J. H.; Kaminski, V. d. L.; Chies, J. A. B. Emerging Infectious Disease Prevention: Where Should We Invest Our Resources and Efforts? *J. Infect. Public Health* **2019**, *12*, 313−316.

(2) Mao, K.; Zhang, K.; Du, W.; Ali, W.; Feng, X.; Zhang, H. The Potential of Wastewater-Based Epidemiology as Surveillance and Early Warning of Infectious Disease Outbreaks. *Curr. Opin. Environ. Sci. Health* **2020**, *17*, 1−7.

(3) Länge, K.; Rapp, B. E.; Rapp, M. Surface Acoustic Wave Biosensors: A Review. *Anal. Bioanal. Chem.* **2008**, *391*, 1509−1519.

(4) Wang, Y.; Wang, H.; Xuan, J.; Leung, D. Y. C. Powering Future Body Sensor Network Systems: A Review of Power Sources. *Biosens. Bioelectron.* **2020**, *166*, 112410.

(5) Kang, M.; Park, E.; Cho, B. H.; Lee, K.-S. Recent Patient Health Monitoring Platforms Incorporating Internet of Things-Enabled Smart Devices. *Int. Neurourol. J.* **2018**, *22*, S76−S82.

(6) Vigneshvar, S.; Sudhakumari, C. C.; Senthilkumaran, B.; Prakash, H. Recent Advances in Biosensor Technology for Potential Applications − An Overview. *Front. Bioeng. Biotechnol.* **2016**, *4*, 11.

(7) Younis, M. R.; Wang, C.; Younis, M. A.; Xia, X.-H. In *Smartphone-Based Biosensors, Nanobiosensors*; Wu, A., Khan, W. S., Eds.; Wiley Online Books, 2020; pp 357−387.

(8) Velusamy, V.; Arshak, K.; Korostynska, O.; Oliwa, K.; Adley, C. An Overview of Foodborne Pathogen Detection: In the Perspective of Biosensors. *Biotechnol. Adv.* **2010**, *28*, 232−254.

(9) Li, Y.; Wang, Z.; Sun, L.; Liu, L.; Xu, C.; Kuang, H. Nanoparticle-Based Sensors for Food Contaminants. *Trac. Trends Anal. Chem.* **2019**, *113*, 74−83.

(10) Wang, Z.; Zhang, J.; Liu, L.; Wu, X.; Kuang, H.; Xu, C.; Xu, L. A Colorimetric Paper-Based Sensor for Toltrazuril and Its Metabolites in Feed, Chicken, and Egg Samples. *Food Chem.* **2019**, *276*, 707−713.

(11) Saleh, T. A.; Fadillah, G.; Saputra, O. A. Nanoparticles as Components of Electrochemical Sensing Platforms for the Detection of Petroleum Pollutants: A Review. *Trac. Trends Anal. Chem.* **2019**, *118*, 194−206.

(12) Van Dorst, B.; Mehta, J.; Bekaert, K.; Rouah-Martin, E.; De Coen, W.; Dubruel, P.; Blust, R.; Robbens, J. Recent Advances in Recognition Elements of Food and Environmental Biosensors: A Review. *Biosens. Bioelectron.* **2010**, *26*, 1178−1194.

(13) Lu, Y.; Zhang, H.; Wang, Z.; Jeong, S.; Jo, M.-C.; Park, M.-H.; Duan, X. Nanoparticle−Membrane Interactions: Real-Time Detection of Nanoparticles Interaction with Lipid Membranes Using an Integrated Acoustical and Electrical Multimode Biosensor (Part. Part. Syst. Charact. 2/2019. *Part. Part. Syst. Char.* **2019**, *36*, 1970004.

(14) Fogel, R.; Limson, J.; Seshia, A. A. Acoustic Biosensors. *Essays Biochem.* **2016**, *60*, 101−110.

(15) Poturnayová, A.; Dzubinová, Ľ.; Buríková, M.; Bízik, J.; Hianik, T. Detection of Breast Cancer Cells Using Acoustics Aptasensor Specific to HER2 Receptors. *Biosensors* **2019**, *9*, 72−87.

(16) Grieshaber, D.; MacKenzie, R.; Vörös, J.; Reimhult, E. Electrochemical Biosensors - Sensor Principles and Architectures. *Sensors* **2008**, *8*, 1400−1458.

(17) Damiati, S.; Schuster, B. Electrochemical Biosensors Based on S-Layer Proteins. *Sensors* **2020**, *20*, 1721.

(18) Pirzada, M.; Altintas, Z. Recent Progress in Optical Sensors for Biomedical Diagnostics. *Micromachines* **2020**, *11*, 356−388.

(19) Chen, C.; Wang, J. Optical Biosensors: An Exhaustive and Comprehensive Review. *Analyst* **2020**, *145*, 1605−1628.

(20) Borisov, S. M.; Wolfbeis, O. S. Optical Biosensors. *Chem. Rev.* **2008**, *108*, 423−461.

(21) Donolato, M.; Antunes, P.; Bejhed, R. S.; Zardán Gómez de la Torre, T.; Østerberg, F. W.; Strömberg, M.; Nilsson, M.; Strømme, M.; Svedlindh, P.; Hansen, M. F.; Vavassori, P. Novel Readout Method for Molecular Diagnostic Assays Based on Optical Measurements of Magnetic Nanobead Dynamics. *Anal. Chem.* **2015**, *87*, 1622−1629.

(22) Schrittwieser, S.; Pelaz, B.; Parak, W.; Lentijo-Mozo, S.; Soulantica, K.; Dieckhoff, J.; Ludwig, F.; Guenther, A.; Tschöpe, A.;

Schotter, J. Homogeneous Biosensing Based on Magnetic Particle Labels. *Sensors* **2016**, *16*, 828−877.
(23) Sepehri, S.; Eriksson, E.; Kalaboukhov, A.; Zardán Gómez de la Torre, T.; Kustanovich, K.; Jesorka, A.; Schneiderman, J. F.; Blomgren, J.; Johansson, C.; Strømme, M.; Winkler, D. Volume-Amplified Magnetic Bioassay Integrated with Microfluidic Sample Handling and High-Tc SQUID Magnetic Readout. *APL Bioeng.* **2018**, *2*, 016102−16112.
(24) Sepehri, S.; Agnarsson, B.; Torre, T. Z. G. d. l.; Schneiderman, J. F.; Blomgren, J.; Jesorka, A.; Johansson, C.; Nilsson, M.; Albert, J.; Strømme, M.; Winkler, D.; Kalaboukhov, A. Characterization of Binding of Magnetic Nanoparticles to Rolling Circle Amplification Products by Turn-On Magnetic Assay. *Biosensors* **2019**, *9*, 109−125.
(25) Khramtsov, P.; Kropaneva, M.; Bochkova, M.; Timganova, V.; Zamorina, S.; Rayev, M. Solid-Phase Nuclear Magnetic Resonance Immunoassay for the Prostate-Specific Antigen by Using Protein-Coated Magnetic Nanoparticles. *Mikrochim. Acta* **2019**, *186*, 768.
(26) Sepehri, S.; Zardán Gómez de la Torre, T.; Schneiderman, J. F.; Blomgren, J.; Jesorka, A.; Johansson, C.; Nilsson, M.; Albert, J.; Strømme, M.; Winkler, D.; Kalaboukhov, A. Homogeneous Differential Magnetic Assay. *ACS Sens.* **2019**, *4*, 2381−2388.
(27) Tian, B.; Gao, F.; Fock, J.; Dufva, M.; Hansen, M. F. Homogeneous Circle-to-Circle Amplification for Real-Time Optomagnetic Detection of SARS-CoV-2 RdRp Coding Sequence. *Biosens. Bioelectron.* **2020**, *165*, 112356−211263.
(28) Oleshkevich, E.; Morancho, A.; Saha, A.; Galenkamp, K. M. O.; Grayston, A.; Crich, S. G.; Alberti, D.; Protti, N.; Comella, J. X.; Teixidor, F.; Rosell, A.; Viñas, C. Combining Magnetic Nanoparticles and Icosahedral Boron Clusters in Biocompatible Inorganic Nanohybrids for Cancer Therapy. *Nanomed. Nanotechnol. Biol. Med.* **2019**, *20*, 101986.
(29) Sharifi, S.; Vahed, S. Z.; Ahmadian, E.; Dizaj, S. M.; Eftekhari, A.; Khalilov, R.; Ahmadi, M.; Hamidi-Asl, E.; Labib, M. Detection of Pathogenic Bacteria via Nanomaterials-Modified Aptasensors. *Biosens. Bioelectron.* **2020**, *150*, 111933.
(30) Berry, C. C. Progress in Functionalization of Magnetic Nanoparticles for Applications in Biomedicine. *J. Phys. D Appl. Phys.* **2009**, *42*, 224003.
(31) Shao, H.; Min, C.; Issadore, D.; Liong, M.; Yoon, T.-J.; Weissleder, R.; Lee, H. Magnetic Nanoparticles and MicroNMR for Diagnostic Applications. *Theranostics* **2012**, *2*, 55−65.
(32) Chen, Y.-T.; Kolhatkar, A. G.; Zenasni, O.; Xu, S.; Lee, T. R. Biosensing Using Magnetic Particle Detection Techniques. *Sensors* **2017**, *17*, 2300−2336.
(33) Huang, H. T.; Garu, P.; Li, C. H.; Chang, W. C.; Chen, B. W.; Sung, S. Y.; Lee, C. M.; Chen, J. Y.; Hsieh, T. F.; Sheu, W. J.; Ouyang, H.; Wang, W. C.; Chang, C. R.; Wang, C. L.; Hsu, M. S.; Wei, Z. H. Magnetoresistive Biosensors for Direct Detection of Magnetic Nanoparticle Conjugated Biomarkers on a Chip. *SPIN* **2019**, *09*, 1940002.
(34) Khan, R.; Rehman, A.; Hayat, A.; Andreescu, S. Magnetic Particles-Based Analytical Platforms for Food Safety Monitoring. *Magnetochemistry* **2019**, *5*, 63−83.
(35) Bychkova, A. V.; Sorokina, O. N.; Rosenfeld, M. A.; Kovarski, A. L. Multifunctional Biocompatible Coatings on Magnetic Nanoparticles. *Russ. Chem. Rev.* **2012**, *81*, 1026−1050.
(36) Fang, C.; Zhang, M. Multifunctional Magnetic Nanoparticles for Medical Imaging Applications. *J. Mater. Chem.* **2009**, *19*, 6258−6266.
(37) Nifontova, G.; Kalenichenko, D.; Baryshnikova, M.; Ramos Gomes, F.; Alves, F.; Karaulov, A.; Nabiev, I.; Sukhanova, A. Biofunctionalized Polyelectrolyte Microcapsules Encoded with Fluorescent Semiconductor Nanocrystals for Highly Specific Targeting and Imaging of Cancer Cells. *Photonics* **2019**, *6*, 117−127.
(38) Akhtar, S.; Strömberg, M.; Zardán Gómez de la Torre, T.; Russell, C.; Gunnarsson, K.; Nilsson, M.; Svedlindh, P.; Strømme, M.; Leifer, K. Real-Space Transmission Electron Microscopy Investigations of Attachment of Functionalized Magnetic Nanoparticles to DNA-Coils Acting as a Biosensor. *J. Phys. Chem. B* **2010**, *114*, 13255−13262.
(39) Lee, W.; Joo, S.; Kim, S. U.; Rhie, K.; Hong, J.; Shin, K.-H.; Kim, K. H. Magnetic Bead Counter Using a Micro-Hall Sensor for Biological Applications. *Appl. Phys. Lett.* **2009**, *94*, 153903.
(40) Wang, S. X.; Guanxiong Li, G. Advances in Giant Magnetoresistance Biosensors With Magnetic Nanoparticle Tags: Review and Outlook. *IEEE Trans. Magn.* **2008**, *44*, 1687−1702.
(41) Lei, Z.; Jian, M.; Li, X.; Wei, J.; Meng, X.; Wang, Z. Biosensors and Bioassays for Determination of Matrix Metalloproteinases: State of the Art and Recent Advances. *J. Mater. Chem. B* **2020**, *8*, 3261−3291.
(42) Astalan, A. P.; Ahrentorp, F.; Johansson, C.; Larsson, K.; Krozer, A. Biomolecular Reactions Studied Using Changes in Brownian Rotation Dynamics of Magnetic Particles. *Biosens. Bioelectron.* **2004**, *19*, 945−951.
(43) Ennen, I.; Hütten, A. Magnetic Nanoparticles Meet Microfluidics. *Mater. Today: Proc.* **2017**, *4*, S160−S167.
(44) Lu, N.; Zhang, M.; Ding, L.; Zheng, J.; Zeng, C.; Wen, Y.; Liu, G.; Aldalbahi, A.; Shi, J.; Song, S.; Zuo, X.; Wang, L. Yolk−Shell Nanostructured Fe3O4@C Magnetic Nanoparticles with Enhanced Peroxidase-like Activity for Label-Free Colorimetric Detection of H2O2 and Glucose. *Nanoscale* **2017**, *9*, 4508−4515.
(45) Strömberg, M.; Zardán Gómez de la Torre, T.; Göransson, J.; Gunnarsson, K.; Nilsson, M.; Svedlindh, P.; Strømme, M. Multiplex Detection of DNA Sequences Using the Volume-Amplified Magnetic Nanobead Detection Assay. *Anal. Chem.* **2009**, *81*, 3398−3406.
(46) de la Torre, T. Z. G.; Mezger, A.; Herthnek, D.; Johansson, C.; Svedlindh, P.; Nilsson, M.; Strømme, M. Detection of Rolling Circle Amplified DNA Molecules Using Probe-Tagged Magnetic Nanobeads in a Portable AC Susceptometer. *Biosens. Bioelectron.* **2011**, *29*, 195−199.
(47) Strömberg, M.; Zardán Gómez de la Torre, T.; Nilsson, M.; Svedlindh, P.; Strømme, M. A Magnetic Nanobead-Based Bioassay Provides Sensitive Detection of Single- and Biplex Bacterial DNA Using a Portable AC Susceptometer. *Biotechnol. J.* **2014**, *9*, 137−145.
(48) Tian, B.; Qiu, Z.; Ma, J.; Zardán Gómez de la Torre, T.; Johansson, C.; Svedlindh, P.; Strömberg, M. Attomolar Zika Virus Oligonucleotide Detection Based on Loop-Mediated Isothermal Amplification and AC Susceptometry. *Biosens. Bioelectron.* **2016**, *86*, 420−425.
(49) Strömberg, M.; Göransson, J.; Gunnarsson, K.; Nilsson, M.; Svedlindh, P.; Strømme, M. Sensitive Molecular Diagnostics Using Volume-Amplified Magnetic Nanobeads. *Nano Lett.* **2008**, *8*, 816−821.
(50) Butterfield, S. M.; Lashuel, H. A. Amyloidogenic Protein-Membrane Interactions: Mechanistic Insight from Model Systems. *Angew. Chem., Int. Ed. Engl.* **2010**, *49*, 5628−5654.
(51) Hu, Y.; Domínguez, C. M.; Bauer, J.; Weigel, S.; Schipperges, A.; Oelschlaeger, C.; Willenbacher, N.; Keppler, S.; Bastmeyer, M.; Heißler, S.; Wöll, C.; Scharnweber, T.; Rabe, K. S.; Niemeyer, C. M. Carbon-Nanotube Reinforcement of DNA-Silica Nanocomposites Yields Programmable and Cell-Instructive Biocoatings. *Nat. Commun.* **2019**, *10*, 5522.
(52) Strömberg, M.; Akhtar, S.; Gunnarsson, K.; Russell, C.; Herthnek, D.; Svedlindh, P.; Nilsson, M.; Strømme, M.; Leifer, K. Immobilization of Oligonucleotide-Functionalized Magnetic Nanobeads in DNA-Coils Studied by Electron Microscopy and Atomic Force Microscopy. *MRS Proceedings*; Materials Research Society, 2011; Vol. *1355*.
(53) Latterini, L.; Tarpani, L. AFM Measurements to Investigate Particulates and Their Interactions with Biological Macromolecules. In *Atomic Force Microscopy Investigations into Biology—from Cell to Protein*; Frewin, L. T. E.-C. L., Ed.; IntechOpen: Rijeka, 2012; pp 87−98.
(54) Perez, J. M.; Josephson, L.; O'Loughlin, T.; Högemann, D.; Weissleder, R. Magnetic Relaxation Switches Capable of Sensing Molecular Interactions. *Nat. Biotechnol.* **2002**, *20*, 816−820.

https://dx.doi.org/10.1021/acssensors.0c01623
ACS Sens. 2020, 5, 3510−3519

(55) Carnerero, J. M.; Jimenez-Ruiz, A.; Grueso, E. M.; Prado-Gotor, R. Understanding and Improving Aggregated Gold Nanoparticle/DsDNA Interactions by Molecular Spectroscopy and Deconvolution Methods. *Phys. Chem. Chem. Phys.* **2017**, *19*, 16113−16123.
(56) Perez, J. M.; Josephson, L.; Weissleder, R. Magnetic Nanosensors for DNA Analysis. *Eur. Cells Mater.* **2002**, *3*, 181−182.
(57) Yan, J.; Hu, C.; Wang, P.; Zhao, B.; Ouyang, X.; Zhou, J.; Liu, R.; He, D.; Fan, C.; Song, S. Growth and Origami Folding of DNA on Nanoparticles for High-Efficiency Molecular Transport in Cellular Imaging and Drug Delivery. *Angew. Chem., Int. Ed.* **2015**, *54*, 2431−2435.
(58) Jiang, Y.; Li, S.; Qiu, Z.; Le, T.; Zou, S.; Cao, X. Rolling Circle Amplification and Its Application in Microfluidic Systems for Escherichia Coli O157:H7 Detections. *J. Food Saf.* **2019**, *39*, No. e12671.
(59) Minero, G. A. S.; Fock, J.; Tian, B.; Rizzi, G.; Neumann, F.; Madaboosi, N.; Nilsson, M.; Fougt Hansen, M. Real-Time Analysis of Switchable Nanocomposites of Magnesium Pyrophosphates and Rolling Circle Amplification Products. *ChemNanoMat* **2020**, *6*, 1276−1282.
(60) Fock, J.; Balceris, C.; Costo, R.; Zeng, L.; Ludwig, F.; Hansen, M. F. Field-Dependent Dynamic Responses from Dilute Magnetic Nanoparticle Dispersions. *Nanoscale* **2018**, *10*, 2052−2066.
(61) Fock, J.; Parmvi, M.; Strömberg, M.; Svedlindh, P.; Donolato, M.; Hansen, M. F. Comparison of Optomagnetic and AC Susceptibility Readouts in a Magnetic Nanoparticle Agglutination Assay for Detection of C-Reactive Protein. *Biosens. Bioelectron.* **2017**, *88*, 94−100.
(62) Reynolds, R. A.; Mirkin, C. A.; Letsinger, R. L. Homogeneous, Nanoparticle-Based Quantitative Colorimetric Detection of Oligonucleotides. *J. Am. Chem. Soc.* **2000**, *122*, 3795−3796.
(63) Foy, C. A.; Parkes, H. C. Emerging Homogeneous DNA-Based Technologies in the Clinical Laboratory. *Clin. Chem.* **2001**, *47*, 990−1000.
(64) Strömberg, M.; Zardán Gómez de la Torre, T.; Göransson, J.; Gunnarsson, K.; Nilsson, M.; Strømme, M.; Svedlindh, P. Microscopic Mechanisms Influencing the Volume Amplified Magnetic Nanobead Detection Assay. *Biosens. Bioelectron.* **2008**, *24*, 696−703.

https://dx.doi.org/10.1021/acssensors.0c01623
ACS Sens. 2020, 5, 3510−3519